Application of two fracture models in impact simulations

T. FRAS[1]*, C.C. ROTH[2], AND D. MOHR[2]

[1] ISL – French-German Research Institute of Saint-Louis, France

[2] ETH Zürich – Department of Mechanical and Process Engineering, Computational Modeling of Materials in Manufacturing, Switzerland

Abstract. The following discussion concerns modelling of fracture in steel plates during an impact test, in which both target and striker are manufactured from the same material, high-strength high-hardness armour steel – Mars® 300. The test conditions (3 mm thick targets, projectiles with different nose shapes at impact velocity lower than 400 m/s) result in severely damaged components, which results in an analysis of stress states showing material failure. Numerical analyses are performed using two material models: the Johnson-Cook approach, as traditionally used in impact simulations, accounting for the effect of stress triaxiality, strain rate and temperature and for comparison, a simulation by means of the stress triaxiality and Lode angle parameter-dependent Hosford-Coulomb model, also incorporating the effect of the strain rate on a fracture initiation. The aim of the study is to analyse the mechanisms of penetration and perforation observed in the armour steel plates and validation of the modelling approaches.

Key words: armour steel, Lode angle parameter, stress triaxiality, Hosford-Coulomb model, Johnson-Cook model.

1. Introduction

Steel grades designed for ballistic protection must be characterized by high strength, high hardness and good ductility, which is required to mitigate kinetic and explosive threats without extensive material loss or brittle failure. An ultra-high hard armour (UHHA) martensitic steel, known under a trade name Mars® 300 belongs to the family of armour steels and in the presented study, its behaviour under impact loadings is tested. The yield strength and ultimate tensile strength of the discussed steel guaranteed by its producer are 1300 MPa and 2200 MPa, and the hardness is close to 640 HB [1]. Mars® 300 steel is available as rolled homogenous plates of different thicknesses and also as plates with a regular circular hole pattern, so-called perforated plates, used as pre-armour add-on ballistic protection [2, 3].

The presented study is complementary to investigations [4] and [5], which were focused on modelling behaviour and failure of Mars® 300 steel plates under impacts by means of a user-defined material model, a combined Swift-Voce/Johnson-Cook plasticity and the Hosford-Coulomb fracture initiation model. The function describing the material is a quadratic plasticity function with a non-associated Hill's 48 flow rule, which couples a Johnson-Cook type of rate- and temperature dependency with a Swift-Voce strain-hardening law. The fracture initiation model accounts for the stress triaxiality and the Lode angle parameter, as well as the strain rate. Recent research on ductile fracture has demonstrated the importance of the effect of the Lode angle parameter [6, 7]. For example, conventional fracture models cannot explain the drop in ductility for biaxial tension

stress states ($0.33 < \eta < 0.667$), while Lode angle-dependent theories, such as the Mohr-Coulomb and Hosford-Coulomb fracture initiation models can accurately describe this phenomenon [8, 9]. The parameters of the models are identified on the basis of a thorough experimental material over a wide range of stress states, temperatures and strain rates. Impact scenarios with perforated and homogenous Mars® 300 plates have already shown that this approach allows a correct modelling of dynamic loads [4, 5].

The impact test campaign in which 3 mm thick steel plates are hit at velocities lower than 400 m/s by projectiles with blunt, conical and hemispherical tips with the mass 14 g is used in numerical analyses with both the aforementioned plasticity and fracture model and using the Johnson-Cook model. This well-known approach is based on phenomenological observations of material deformation and it accounts for the stress triaxiality, the strain rate and temperature in the functions of plasticity and fracture [10, 11]. Numerous examples show that this model provides a reasonable simulation of impact damage and a good prediction of residual velocity, e.g. [12–14].

Different geometries of projectile's tip impose a particular stress state in the impacted target, therefore such tests are often analysed numerically to validate plasticity and fracture models implemented in FEM solvers. The aim of this work is a numerical simulation of interactions between the target/threat configurations resulting in an analysis of the observed failure modes, which validate the used modelling approaches.

2. Impact tests

Already in early works which concerned impact problems, it was observed that the mechanisms of impact energy absorption and ultimate failure are dependent on a projectile/target config-

T. Fras, C.C. Roth, and D. Mohr

uration [15–17]. In academic studies, strain-stress states leading to various failures are imposed in targets by strikers with different tips. Generally, it was observed that in configurations of rigid strikers/thin ductile metallic targets, blunt projectiles cause the failure of plates by plugging, sharp-nosed projectiles by petalling, and hemispherical ones by a ductile hole enlargement. Various target configurations have been tested against these three basic types of projectiles, e.g. [12–14]. With the development of numerical methods, experimental observations are complemented by numerical simulations providing insight into local fields. In most studies, projectiles of about 12 g are shot at a velocity of 50–400 m/s achievable by means of single-stage gas guns in laboratory conditions. Limitations of experimental stands influence the choice of the striker/target configurations and their material and geometrical properties. In the hereby presented study, a series of impacts are analysed to provide an insight into the governing mechanisms leading to the perforation of ultra-hard high strength steels. Both the strikers and targets are extracted from an armour grade steel; in consequence, due to the contract they undergo deformation, which is modelled by numerical simulations carried out to validate the plasticity and fracture models.

The impact tests are conducted by means of a high-pressure single-stage gas gun presented in Fig. 1. Helium gas is used as the propellant provides a maximum admissible pressure of 80 bar. The highest possible impact velocity for strikers with the given mass close to 14 g reaches 380 m/s. The impact velocity is measured by a double-laser light barrier located near the exit of the gun muzzle, Fig. 1. Impacts are also registered by a Shimadzu HPV1 high-speed camera, due to which the projectile's trajectory is followed before and after plate perforation.

In the test configuration, projectiles with blunt, hemispherical and conical noses cut by a wire EDM from the steel plates
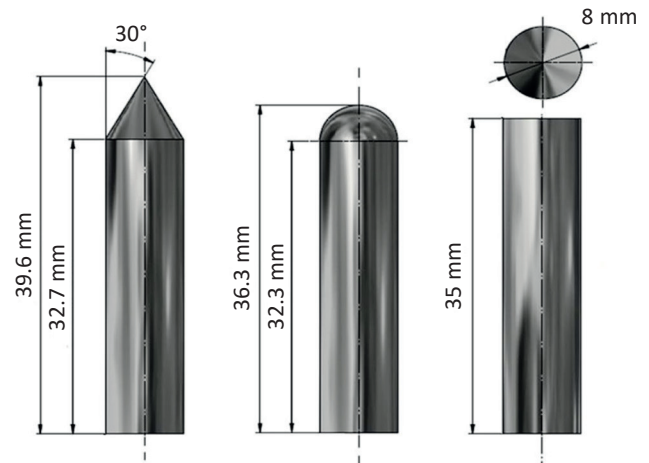

Fig. 2. Geometries of projectiles shot in the impact test

with the initial thickness of 12 mm are shot. Projectiles have the same mass of 13.8 g and diameter of 8 mm, which results in different lengths; i.e. 39.6 mm, 36.3 mm and 35 mm for the conical, hemispherical and blunt striker (Fig. 2).

The thinnest Mars® 300 plates available on the market have a thickness of 6 mm. To ensure that strikers of the given mass perforate the plates at maximum possible velocity, the initial plate thickness is reduced by grinding from only one side under permanent cooling to prevent changes of the microstructure. Final target size is then 120×120 mm, with thickness of 3 mm. When thin ductile targets are impacted by projectiles which remain rigid after plate perforation, the final plate failure modes are strongly affected by the projectile tip geometries and they differ significantly depending on the tip shape. In the discussed examples, differences between observed perforation modes are not so distinct but still, the resulted failure modes differ slightly depending on the tip shape. The ductility of the armour steel is too low to observe modes with various features, such as petals.

It is observed that the plates fail due to plugging when the conical and hemispherical projectile hit the plates, whereas the blunt projectiles at the highest possible impact velocity do not cause plate perforation (Fig. 3). Blunt projectiles punch regular, localized bulges of the diameter close to that of the striker. Hemispherical and conical strikers ejected plugs and some smaller debris in a ring shape with a thickness of approximately 1.5 mm and diameter of ca. 7.7–8 mm. The exit holes, remaining after the passage of the conical impactors, are more irregular with sharp edges. The hemispherical impactor causes regular circular hole. The holes created by the projectiles are slightly larger than the projectiles' diameter (8.3–8.8 mm).

Contact with the targets also causes damage on the projectiles. An initially pointed nose of the conical projectiles is reduced, affecting the size of the plugs. The noses of hemispherical projectiles deform to a smaller extent, so the shape of plugs is similar at all impact velocity with the diameter close to 4.6 mm. Due to the impacts at the velocity of 290 m/s, the projectiles lengths are reduced to 35.86 mm and to 36.01 for the hemispherical and conical tips. The blunt projectiles are reduced in length by 3.4 mm.
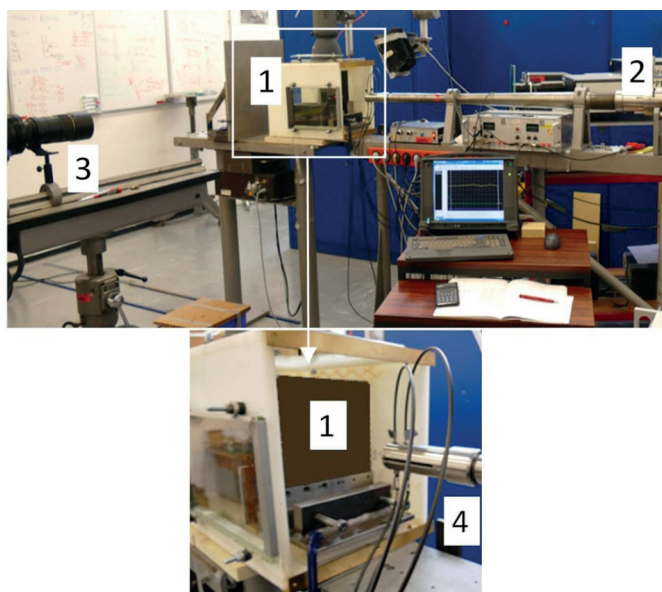

Fig. 1. Test set-up: [1] specimen mounted in the catch box, [2] single-stage gas gun, [3] high-speed camera for the side view, [4] gun barrel with a double-laser light barrier
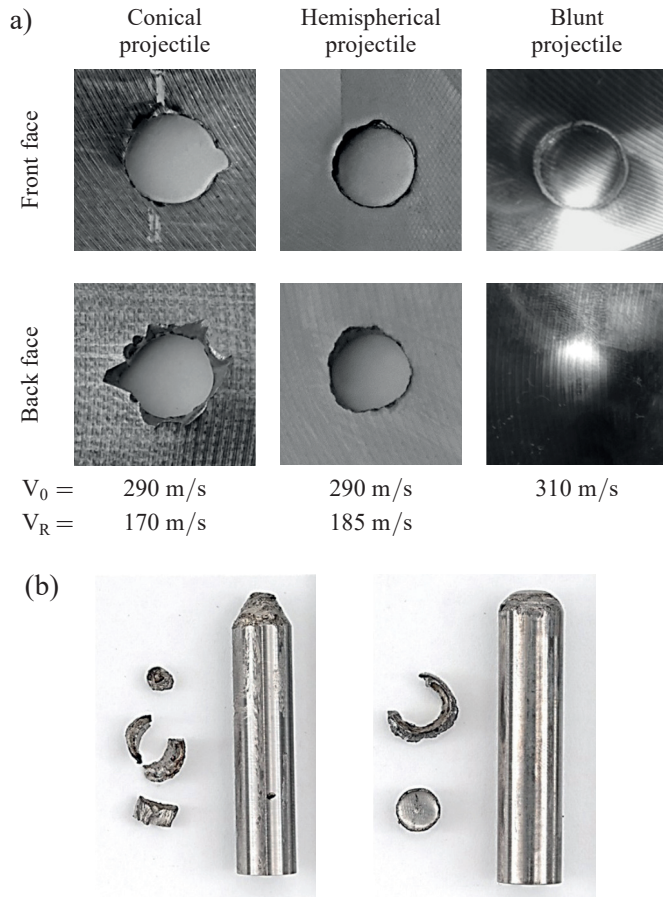
a)

Fig. 3. (a) Perforation holes in 3 mm thick steel plates and (b) conical and hemispherical projectiles after the impacts (V_0 – initial impact velocity, V_R – residual velocity after plate perforation)

3. Numerical simulations and their results

A numerical simulation is undoubtedly a useful tool providing a detailed analysis of material behaviour, which may lead to a better understanding of the target response to impacts on condition that the simulation is carefully prepared and the chosen material model is based on proper material characterization. Because of strong deformation, strain localization, increase of strain rate and temperature and the final fracture in the interacting materials, simulations of impacts still represent a challenge and may be approached by different numerical techniques.

The Lagrangian finite element formulation is the most intuitive, as it represents the experimental configuration by a deformable geometry, it has many implemented material models and numerous examples describe its successful applications. The FEM Lagrangian approach is not free from shortcomings, which is noticeable especially in modelling of strong deformation and failure. The FEM Lagrangian model in the impact zone should have a fine mesh allowing element removal along the perforation path. To represent fracture, the technique of distorted element deletion must be applied in the code, which is often criticized as a purely numerical manipulation. There are some other numerical approaches which offer alternative solu-

tions in simulating impact problems, for example the smoothed particle hydrodynamics (SPH) meshless Lagrangian method or the arbitrary Lagrange-Eulerian (ALE) method [18–20]. In the SHP approach, the material geometry is discretized by a number of nodes, representing particles to which material characteristics are assigned. In comparison to FEM, the major advantage of SPH is material deformation without severe mesh distortion – no algorithm of element erosion is then required. On the other hand, some authors signal problems of improper material failure modelling, it is also noticed that the SPH method may be computationally less efficient comparing to standard Lagrangian calculations and that it suffers from certain instability problems [21]. In the ALE description, the nodes of the computational mesh may be moved with the continuum in normal Lagrangian fashion, or be held fixed in Eulerian manner, [22]. The ALE modelling offers more freedom in moving the computational mesh, so greater distortions of the continuum can be handled better than it would be allowed by a purely Lagrangian method, with more resolution than that afforded by a purely Eulerian approach. Since the domain representation in two types of descriptions may not be evident, not all impact problems may be properly represented by the ALE approach.

In the current study, the FEM Lagrangian is applied, which together with the chosen material modelling allows an analysis of the discussed impact event. The calculations are carried out using the explicit solver of the finite element software package LS-Dyna R9.0.1 [23]. Assuming the symmetry of the modelled configuration, only one quarter has been implemented into the calculations, Fig. 4.

The target plate and projectiles are meshed with reduced integration 8-node solid elements with stiffness-based hourglass control. The impact zone in the target and the tip of the projectile are discretized with a fine mesh of element edge
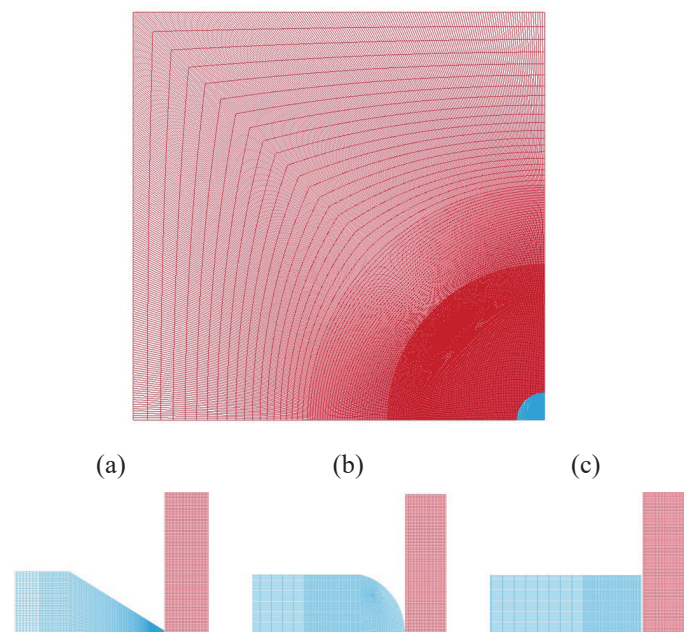

Fig. 4. Mesh of the numerical configuration. Cross-section of the impact zone with:(a) conical, (b) hemispherical and (c) blunt projectiles

length 0.1 mm. The validation of the plasticity and fracture models, discussed in [5], is performed based on the simulation of uniaxial tests of samples meshed by elements with this edge size. The target plate has 30 elements through the plate thickness and a refined mesh in a diameter of 20 mm around the centre. The next zone of length 12 mm consists of elements with edge length 0.4 mm and finally, on the plate edges there are the largest elements with the edge length of 2 mm (Fig. 4). In total, the quarter of the target plate is meshed by 1.5 million elements. The front part of the impactors is also meshed with 0.1×0.1×0.1 mm elements; the part not affected by the contact with the target plate is meshed by elements with length 1 mm – which results in almost 300,000 elements for each projectile. Besides symmetry conditions, boundary conditions are applied to the plate and it is constrained at its top and bottom edges. The impact velocity is imposed on the striker as the initial condition. As there is no experimental insight into the friction conditions between the targets and projectiles, the conservative assumption of frictionless contact between them is adopted. To impose erosion of ultimately distorted elements, the contact definition *ERODING_SURFACE_TO_SURFACE available in the program is applied. In the Ls-Dyna software, the eroding contact types are used when solid elements involved in the contact are subjected to deletion due to material failure criteria. These eroding contacts contain logic which allows the contact surfaces to be updated as exterior elements are deleted [23].

3.1. Material characterization. The producer of the steel provides information about general material properties, [1]. However, to understand the material behaviour and to calibrate material models necessary for numerical simulation, a more detailed material characterization is required. The armour steels are thus tested under different loading and temperature conditions, see the discussion in [5].

The basic testing program for calibrating the material models included six different types of specimen geometries, Fig. 5, which impose in the material the following state of stresses: uniaxial tension, different stress triaxiality factors obtained by tensile notched samples, shearing, a plane strain tension bending and finally, an equi-biaxial loading.

The following specimen types are extracted from plates ground to 1 mm thickness:
- uniaxial tension (UT) specimens with a 5 mm wide and 20 mm long gage section area,
- notched tensile specimens (NT10) with a 10 mm wide gage section and circular cut-outs with a notch radius of R = 10 mm (NT10), reducing the width of the gage section to 5 mm in the centre,
- mini-punch (PU) specimens with a diameter of 60 mm, to characterize the material response under equi-biaxial loading,
- shear (SH) specimens featuring a single gage section,
- strip specimens for plane strain tension bending (Bend) experiments.

In the tests, the strain field is monitored by digital image correlation. The strain and stress fields inside the specimens are identified through a hybrid-experimental-numerical approach,
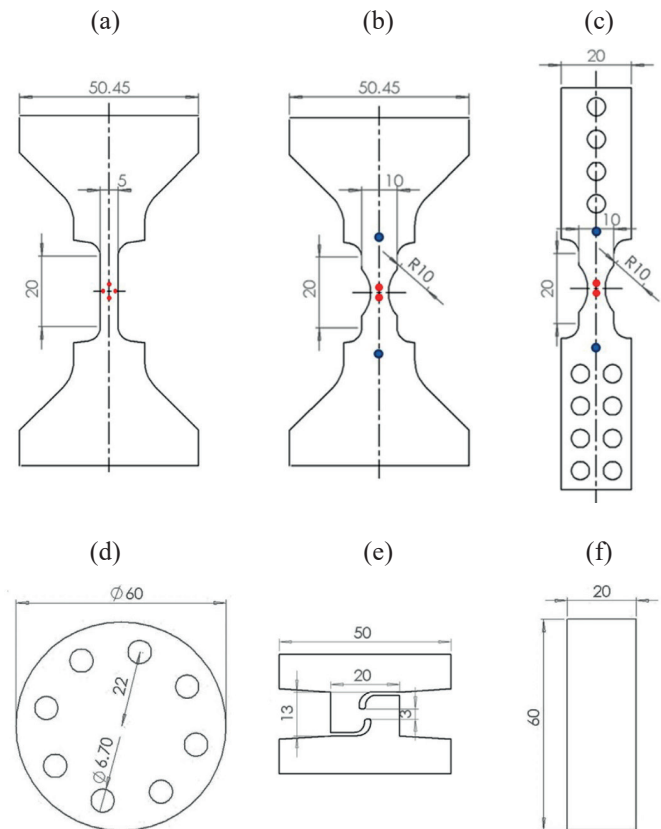

Fig. 5. Specimen geometries for calibration of the SV–HC plasticity and fracture models: a) tensile specimen, b) notched tensile specimen, c) specimen for dynamic loading, d) mini-punch specimen, e) shear specimen and f) bending specimen

which involves the FEA modelling of all experiments with 3D solid element meshes.

As can be seen in Fig. 6a, the true-stress-plastic strain response along the 0°, 45° and 90° direction revealed no significant difference in the yield point $\sigma_Y = 1380$ MPa which allows an application of the von Mises yield surface. The material exhibits a moderate strain rate hardening behaviour. Figure 6b shows the material response for three selected strain rates.

In the triaxiality range of $1/3 \leq \eta \leq 2/3$, a minimum in material ductility is observed for the uniaxial tension and steep gradients exist towards uniaxial and biaxial tension, as shown in the fracture curve being a cross-section in the space of stress triaxiality, the equivalent plastic strain and the Lode angle parameter (Fig. 6). The equivalent strains reached about 0.4, 0.18 and 0.35 in the shear, plane strain tension and equi-biaxial tension experiments, respectively.

3.2. The Swift-Voce Hosford-Coloumb approach. In the first proposed numerical approach, a linear combination of a power law [30] and a saturation law [31] is applied in order to capture the strain hardening behaviour. The effects of the strain rate and temperature are incorporated in a multiplicative manner, inspired by the work of Johnson and Cook [22–23]. The stress-triaxiality, Lode angle parameter and strain-rate depen-
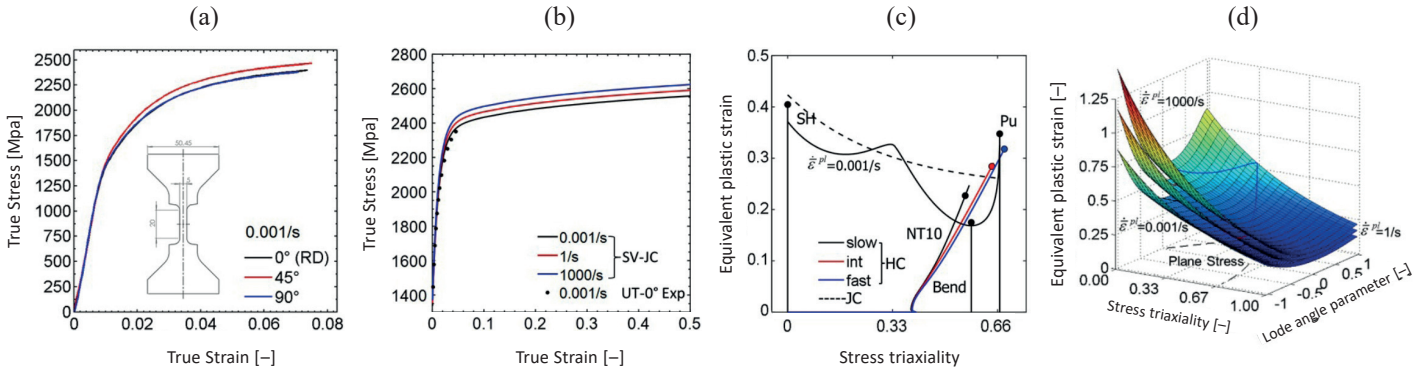
Fig. 6. Response of the Mars® 300 steel: a) true stress vs. logarithmic strain curves in tension and b) inter- and extrapolation of the calibrated hardening law at different strain rates, c) the fracture envelope corresponding to the strain rate 0.001 s⁻¹, d) illustration of the fracture surfaces in the space of stress triaxiality, Lode angle parameter and equivalent plastic strain. JC – Johnson-Cook fracture model, HC – Hosford-Coulomb fracture model. By circular points the experimental results are denoted for: UT – uniaxial tension, NT10 – tension with tensile notched samples, SH – shearing, Bend – bending, PU – equi-biaxial loading

dent Hosford-Coulomb fracture initiation model is used to predict the material failure. Based on unit cell analyses [10, 11], the Hosford-Coulomb fracture initiation model assumes that ductile fracture is imminent with the onset of shear localization at the micro-scale.

The stress triaxiality η and the Lode angle parameter $\bar{\theta}$ are defined as follows:

$$\eta = \frac{I_1}{3\sqrt{3J_2}} \tag{1}$$

$$\bar{\theta} = 1 - \frac{2}{\pi}\arccos\left[\frac{3\sqrt{3}}{2}\frac{J_3}{(J_2)^{3/2}}\right] \tag{2}$$

with $I_1 = tr\boldsymbol{\sigma}$, $J_2 = \frac{1}{2}\mathbf{s}:\mathbf{s}$, $J_3 = det[\mathbf{s}]$ and $\mathbf{s} = dev[\boldsymbol{\sigma}]$.

The equivalent plastic strain to failure for a proportional loading then reads:

$$\bar{\varepsilon}_f^{pr}(\eta, \bar{\theta}, \dot{\bar{\varepsilon}}_p) = f_1 - f_2^a$$

$$b(1+c)^{\frac{1}{n}}\left[\left\{\frac{1}{2}\left((f_1-f_2)^a + (f_2-f_3)^a + (f_3-f_1)^a\right)^{\frac{1}{a}}\right\}^{-\frac{1}{n}} + c(2\eta + f_1 + f_3)\right] \tag{3}$$

The function is a dependence of the stress triaxiality η, the Lode angle parameter $\bar{\theta} \in [-1, 1]$ and $\dot{\bar{\varepsilon}}_p$ – the strain rate. The Lode angle parameter depends on trigonometric functions:

$$f_1(\bar{\theta}) = \frac{2}{3}\cos\left[\frac{\pi}{6}(1-\bar{\theta})\right],$$

$$f_2(\bar{\theta}) = \frac{2}{3}\cos\left[\frac{\pi}{6}(3+\bar{\theta})\right], \tag{4}$$

$$f_3(\bar{\theta}) = \frac{2}{3}\cos\left[\frac{\pi}{6}(1+\bar{\theta})\right].$$

The main model parameters are $a(\bar{\theta})$, $b(\dot{\bar{\varepsilon}}_p)$, $c(\eta)$. The parameter $a(\bar{\theta})$ (the Hosford exponent, $1 \leq \eta \leq 2$) controls the influence of the Lode angle parameter, while the friction coefficient $c(\eta)$ describes the influence of the stress triaxiality. The effect of the strain rate is incorporated into the model through the function $b(\dot{\bar{\varepsilon}}_p)$.

$$b(\dot{\bar{\varepsilon}}_p) = \begin{cases} b_0 & for\ \dot{\bar{\varepsilon}}_p < \dot{\varepsilon}_0 \\ b_0\left(1+\gamma\ln\left[\frac{\dot{\bar{\varepsilon}}_p}{\dot{\varepsilon}_0}\right]\right) & for\ \dot{\bar{\varepsilon}}_p \geq \dot{\varepsilon}_0 \end{cases}, \tag{5}$$

Where $b_0 > 0$ is the strain to fracture for uniaxial tension at the reference strain rate $\dot{\varepsilon}_0$, and the model parameter $\gamma \geq 0$ controls the strain rate sensitivity of the fracture initiation model. The parameter b describes the overall ductility of the material and is defined so as to correspond to the strain to fracture for uniaxial (or equi-biaxial) tension for equivalent plastic strain rates that are lower than the reference strain rate $\dot{\varepsilon}_0$.

Using a damage indicator framework with linear damage accumulation, the onset of fracture is described through element deletion once the following condition is met:

$$\int_0^{\bar{\varepsilon}_f} \frac{d\bar{\varepsilon}_{pl}}{\bar{\varepsilon}_f^{pr}[\eta, \bar{\theta}, \dot{\bar{\varepsilon}}_p]} = 1 \tag{6}$$

For plane stress conditions, the Lode angle parameter can be expressed as a function of the stress triaxiality:

$$\bar{\theta} = 1 - \frac{2}{\pi}\arccos\left[-\frac{27}{2}\eta\left(\eta^2 - \frac{1}{3}\right)\right] \tag{7}$$

for $-2/3 \leq \eta \leq 2/3$.

The equivalent strains reaching 0.4, 0.18 and 0.35 in the states of shear, plane strain tension and equi-biaxial tension is presented in Fig. 6c. A steep gradient exists in the Lode angle parameter from $\bar{\theta} = 1$ for the uni-axial tension to $\bar{\theta} = -1$ for the equi-biaxial tension.

T. Fras, C.C. Roth, and D. Mohr

In the numerical simulation, the aforementioned plasticity and fracture models are implemented by the UMAT subroutine, but this model could also be used through *MAT_260B in Ls-Dyna packages. Application of this material model does not require an equation of state, neither additional add-erosion criterions. The model's parameters may be found in the precedent works [4, 5].

The simulation reveals that the target deformation changes according to the striker geometry, even if differences are not as distinct as during perforation of less hard metals. The exit of the hemispherical projectile is smoother, while the blunt projectile left a circular imprint on the front side of the plate. The plastic deformation and the erosion of the tips of all three projectiles are accurately represented in the simulation.

The numerical model also predicts the formation of plugs whose shapes are similar to those observed experimentally. The plugs are slightly less compressed (2.6 mm as compared to 2.4 mm measured in the experiment) and their diameters are larger, which is a consequence of the inaccurate modelling of the secondary debris ejected from the plates in the experiments. The projectile velocity according to the simulation drops to 165 m/s and to 155 m/s for the hemispherical and the conical striker, respectively. As in the experiment, the blunt striker does not perforate the plate – its trace left on the front plate face, as well its deformation is well represented in the simulation.

An acceptable agreement between the numerical results and the experimentally observed shapes of the target, projectiles and ejected debris is obtained, as shown in Fig. 7. The residual velocities calculated numerically are 10% underestimated (c.f. [4]) but in all cases, due to the modelling approach used, the main geometrical features and differences between the deformed tests' components are featured. The presented simulation does not result in a perfect mirroring of the performed impacts but it captures experimentally observed sensitivities in deformation and damage of three tested cases. It is a much more sophisticated analysis than just a simple "hole–no hole" evaluation, still promoted in some numerical studies.

3.3. The Johnson-Cook approach.

The Johnson-Cook plasticity and fracture model is implemented in most commercial computer codes. It is based on a von Mises yield surface and flow rule in conjunction with a power-law strain hardening, as well as multiplicatively added strain rate hardening and temperature softening terms [10, 11]. The individual expressions in the three sets of brackets represent the strain hardening, strain rate hardening and thermal softening, and can be calibrated separately using experimental data presented as stress-strain curves at different strain rates and temperatures. However, it should be noted that despite its success and simplicity, the JC model is not based on physics of materials, but on phenomenological observations of their behaviour.

The plasticity model given in Equation (8) is developed for isotropic materials and includes visco-plasticity and ductile damage. The elastic and visco-plastic properties of the material depend on the temperature generated by adiabatic heating under high strain-rate loading conditions, while any thermo-mechanical coupling with the surroundings is not included in the
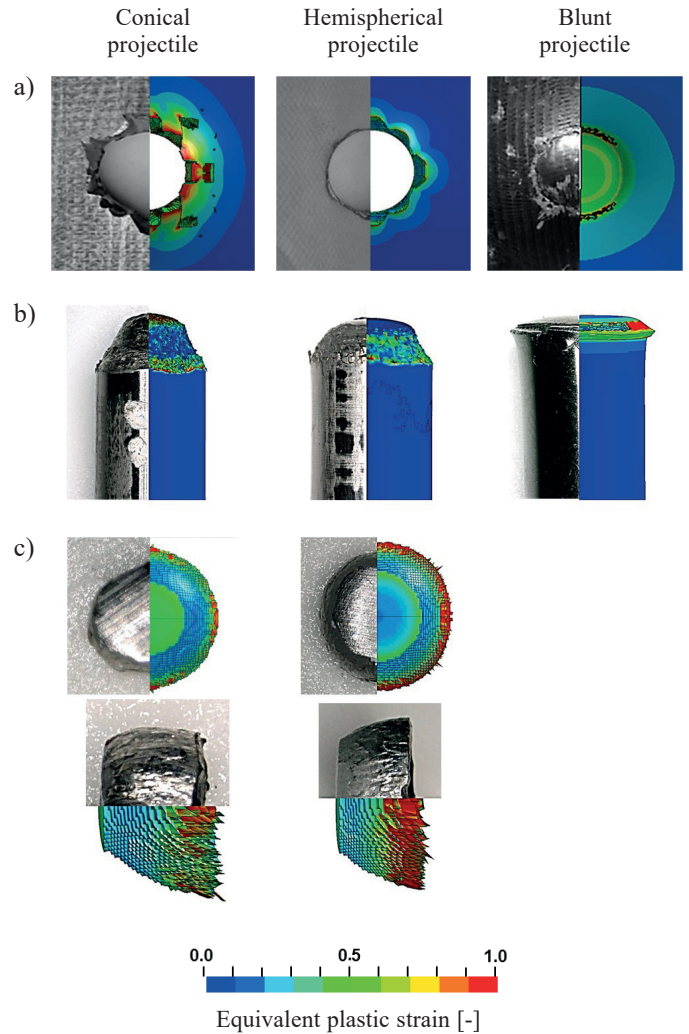

Fig. 7. Results of the Hosford-Coulomb fracture modelling. Comparison of geometrical characteristics of (a) exit holes (entry holes in the case of the blunt striker), (b) projectiles and (c) plugs remained after passage of impactors at impact velocity 290 m/s

formulation. Strain hardening is thus described in terms of the damage accumulated plastic strains.

$$\sigma\left(\varepsilon, \dot{\varepsilon}, T\right) = \left(A + B\varepsilon^{n}\right)\left(1 + C\ln\dot{\varepsilon}^{*}\right)\left(\frac{T - T_{room}}{T_{melt} - T_{room}}\right)^{m} \quad (8)$$

where A, B, C, m, n are material constants.

The function describing the fracture proposed by Johnson and Cook strain depends on the stress triaxiality, strain rate and temperature. The strain at fracture is given by:

$$\varepsilon_{f}\left(\eta, \dot{\varepsilon}, T\right) = \frac{\left[D_{1} + D_{2}expD_{3}\eta\right]\left[1 + D_{4}\ln\varepsilon^{n}\right]}{\left[1 + D_{5}\dfrac{T - T_{room}}{T_{melt} - T_{room}}\right]} \quad (9)$$

where ε_{f} is the equivalent plastic fracture strain, $D_{1} - D_{5}$ are fracture model constants. The damage evolution is described

by the damage variable D, representing the surface density of intersections of micro-cracks and micro-cavities with any plane in the body. For material in initial state of loading D = 0 and for a material which failed fully D = 1. Fracture occurs when the damage parameter D reaches 1:

$$D = \sum \frac{\Delta \varepsilon}{\varepsilon_f}. \tag{10}$$

The parameters of the Johnson-Cook model are identified based on the experimental data and the least-squares fitting algorithm (see Fig. 6c), as shown in Table 1.

Table 1
The parameters of the Johnson-Cook plasticity and fracture models

$\rho\,[\mathrm{kg/m^3}]$	$G\,[MPa]$	$E\,[MPa]$	$T_{ref}\,[°C]$	$T_m\,[°C]$
7850	70	200	25	1287
$A\,[MPa]$	$B\,[MPa]$	C	n	m
1400	1550	0.15	0.168	1.39
D_1	D_2	D_3	D_4	D_5
0.24	0.25	−3.27	0.04	0.0

In the calculations, the Johnson-Cook models are implemented by the *MAT_15 card – one of several Johnson–Cook formulations available in the Ls-Dyna software. This particular model option is often chosen by users because it incorporates the original functions proposed in [10, 11]. However, regardless of type and rates of loading, this model requires an equation-of-state when used with solid elements [23]. The equation of state is accounted through *EOS_Gruneisen with parameters suitable for steel 4340 [24, 25].

The simulation with the JC model is performed using the same numerical configurations (geometry, number of elements, contact options and impact velocity) as described previously.

Hemispherical projectile   Blunt projectile

0.0   0.5   1.0
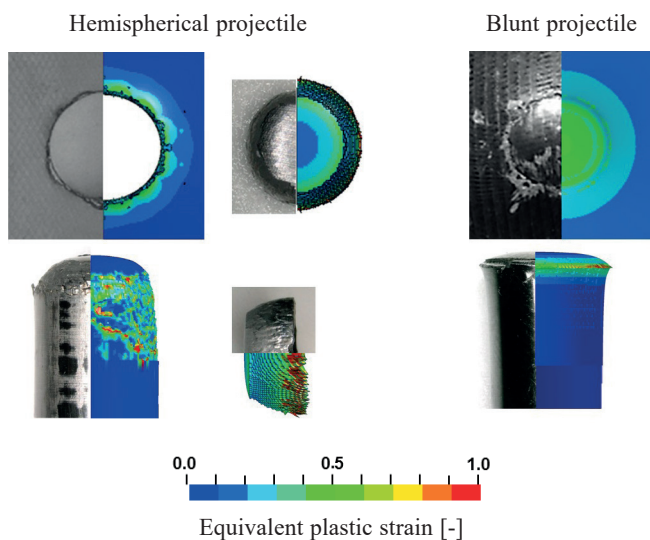Equivalent plastic strain [-]

Fig. 8. Results of the impact simulations with the Johnson-Cook model

The results obtained by means of the JC material model for the hemispherical and blunt strikers are shown in Fig. 9. The conical impact case was not simulated successfully because of numerical problems in contact between the pointed-nosed striker and the target, which was not kept correctly through the entire simulation.

7.5 µs   8.5 µs   11.5 µs   12.5 µs

0.0   0.5   1.0
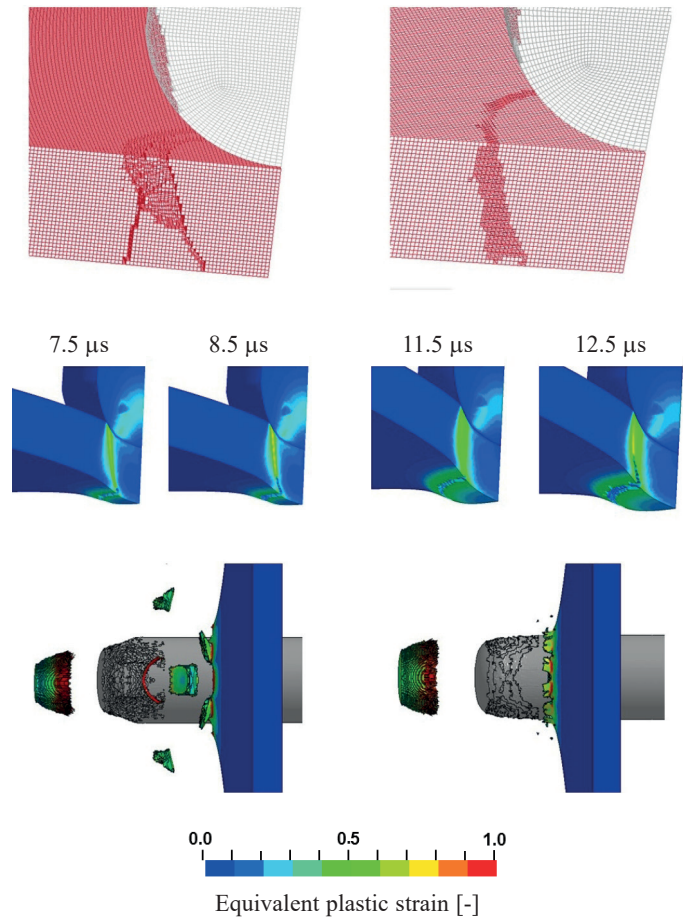Equivalent plastic strain [-]

Fig. 9. Comparison between the fracture modelling with the Hosford-Coulomb and the Johnson-Cook approaches: (a) the crack paths, (b) the crack initiation and (c) the side view of the perforated configurations

Deformation of the projectiles is modelled slightly differently when compared to the previous modelling approach. A plug ejected by the hemispherical striker is larger than its experimental equivalent, since the secondary debris is not modelled at all (Fig. 8), but the dominant failure mode is correctly visualized. The calculated residual velocity of the round projectile is lower than in the experiment, it drops to 155 m/s. The plate struck by the blunt projectile is not perforated, which is modelled as it was observed in the experiment.

Figure 9 presents a comparison between the perforation modes obtained by two used modelling methods. The lack of secondary debris in the JC approach is the most striking difference; different plug sizes, as well as a range of projectile tip deformation, are also noticeable.

When comparing the mechanism of fracture development in two discussed modelling approaches, it is observed that the Johnson-Cook model determines a crack initiation 4 μs later than the Hosford-Coulomb model (Fig. 10b). In both cases, the fracture starts at the rear plate side and propagates to its front face. In the JC visualisations of target deformation, the shear band which preceeds the crack is wider than the more localized band in the HC modelling. Both computational approaches result in the generally similar target failures, but when taking a closer look, these two solutions have certain differences.
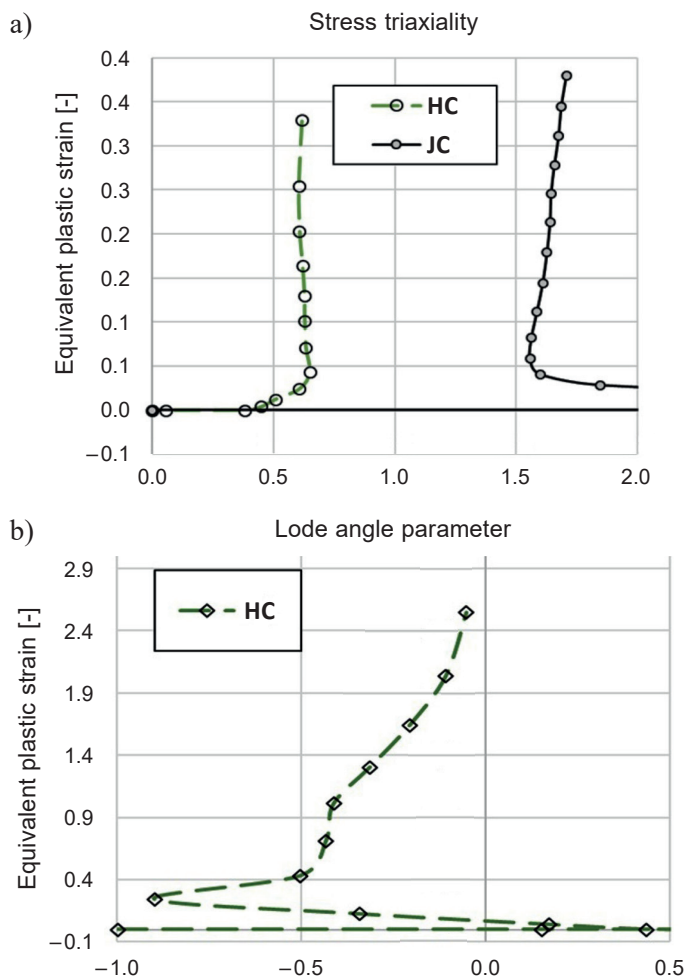
a)

b)

Fig. 10. Stress triaxiality (a) and (b) Lode angle parameter for the element which eroded as the first

The HC approach allows a more detailed description of the stress state. The loading paths to fracture for the first deleted element reveals an almost perfectly proportional loading path close to a plane strain tension stress state with the stress triaxiality close to 0.58 and Lode angle parameter reaching 0.

The loading paths to fracture for the element that failed first differ between the two models. Nonetheless, both models show that the bottom element fails in a tensile stress state from the back face of the plate, Fig. 10a. The stress triaxiality calculated by the JC model increases greatly above values representative

for biaxial tension, while a complementary analysis of the Lode angle parameter is not possible since the JC model does not account for this parameter.

4. Conclusions

Stress states occurring in the impact zone are complex and accompanied by an increase in strain rates and temperature during penetration. Models used in an impact simulation must represent these evolving conditions if fracture leading to plate penetration was correctly predicted. Failure modes in Mars® 300 steel plates resulting from the impacts have been modelled by means of the classical Johnson-Cook model and the Hosford-Coulomb fracture initiation model. As discussed in the previous sections, both modelling methods result in a simulation which is applicable to analyse penetration and perforation process occurring in the impacted steel.

During the perforation of the 3 mm thick steel plate, fracture initiates at the back face of the plate under biaxial tension, while the cracks propagate through the band of localized plastic deformation towards the impacted front face of the plate, forming a plug. As the targets are made from high-strength steel, the projectiles deform during penetration, resulting in an ovoid shape similar to the hemispherical tip. Other failure modes are observed neither in the experiment, nor in the simulation approach.

Comparing to the SV–HC modelling, the JC calculations present a more ambiguous material response – the classical approach does not cover all sensitivities of the material deformation occurring during impacts. The application of the Lode angle parameter in the calculations seems to increase the modelling accuracy. The evolution of the local mechanical fields during the perforation processes can be analyzed more specifically when secondary debris is formed.

Comment: Since the 1st of May 2019, the steel grades Mars® have had redesigned names, and the hardness in Brinell characteristic has been followed for the grade. In the new designation, Mars® 650 grade is a specific version of the former Mars® 300.

REFERENCES

[1] Industeel Brochure. MARS® 300 perforated MARS®300. France: Industeel; 2015 November.

[2] T. Fras, A. Murzyn, and P. Pawlowski, "Defeat mechanisms provided by slotted add-on bainitic plates against small-calibre 7.62 mm×51 AP projectiles", *Int. J. Impact Eng.* 103, 241–53 (2017).

[3] T. Fras and N. Faderl, "Influence of add-on perforated plates on the protective performance of light-weight armour systems", *Problems of Mechatronics. Armament, Aviation, Safety Eng.* 9.1.13, 31–48 (2018).

[4] T. Fras, C.C. Roth, and D. Mohr, "Dynamic Perforation of Ultra-hard High-Strength Armour Steel: Impact Experiments and Modelling", *Int. J. Impact Eng.* 131, 256–71 (2019).

[5] T. Fras, C.C. Roth, and D. Mohr, "Fracture of high-strength armour steel under impact loading",*Int. J. Impact Eng.* 111, 147–64 (2018).

[6] C.C. Roth and D. Mohr, "Effect of Strain Rate on Ductile Fracture Initiation in Advanced High Strength Steel Sheets: Experiments and Modelling", *Int. J. Plasticity* 56, 19–44 (2014).

[7] C.C. Roth and D. Mohr, "Ductile fracture experiments with locally proportional loading histories", *Int. J. Plasticity* 79, 328–54 (2016).

[8] M. Dunand and D. Mohr, "Effect of Lode parameter on plastic flow localization after proportional loading at low stress triaxialities", *J. Mech. Physics Solids.* 66, 133–53 (2014).

[9] D. Mohr and J.C. Marcadet, "Micromechanically-motivated Phenomenological Hosford-Coulomb Model for Predicting Ductile Fracture Initiation at Low Stress Triaxialites", *Int. J. Solids Structures,* 67–68, 40–55 (2015).

[10] G.R. Johnson and W.H. Cook, "A constitutive model and data for metals subjected to large strains, high strain rates and high temperatures", in: *Proceed 7ᵗʰInt. Symp. on Ballistics IBS. The Hague*; 541–7 (1983).

[11] G.R. Johnson and W.H. Cook, "Fracture characteristics of three metals subjected to various strains, strain rates, temperatures and pressures", *Eng. Fract. Mech.* 21, 31–48 (1985).

[12] T. Børvik, M. Langseth, O.S. Hopperstad, and K.A. Malo, "Ballistic penetration of steel plates", *Int. J. Impact Eng.* 22(9), 855–86 (1999).

[13] T. Børvik, M. Langseth, O.S. Hopperstad, and K.A. Malo, "Perforation of 12 mm thick steel plates by 20 mm diameter projectiles with flat, hemispherical and conical noses: part I: experimental study", *Int. J. Impact Eng.*27(1), 19–35 (2002).

[14] T. Børvik, M. Langseth, O.S. Hopperstad, and K.A. Malo, "Perforation of 12 mm thick steel plates by 20 mm diameter projectiles with flat, hemispherical and conical noses: part II: numerical simulations", *Int. J. Impact Eng.* 27(1), 37–64 (2002).

[15] J. Awerbuch, "A mechanics approach to projectile penetration", *Technion-Israel Inst of Tech Haifa*; 1970.

[16] W. Golsdmith and S.A. Finnegan, "Penetration and perforation processes in metal targets at and above ballistic velocities", *Int. J. Mech. Sci.* 13(10), 843–66 (1971).

[17] R.L. Woodward and M.E. De Morton, "Penetration of targets by flat-ended projectiles", *Int. J. Mech. Sci.* 18(3), 119–27 (1976).

[18] L.E. Schwer and C. A.Windsor, "Aluminum Plate Perforation: A Comparative Case Study Using Lagrange With Erosion, Multi-Material ALE, and Smooth ParticleHydrodynamics", Proceedigns 7th European LS-DYNA conference 2009.

[19] M. Becker, M. Seidl, M. Mehl, and M.Souli, "Numerical and Experimental Investigation of SPH, SPG, and FEM for High-Velocity Impact Applications", Proceedigns of 12th European LS-DYNA Conference 2019.

[20] T. Fras, L. Colar, and P. Pawlowski, "Perforation of aluminum plates by fragment simulating projectiles (FSP)", *Int. J. Multiphysics.* 9(3), 267–86 (2015).

[21] S.M. Swaddiwudhipong, J. Islamb, and Z.S. Liu, "High velocity penetration/perforation using coupled smooth particle hydrodynamics-finite element method", *Int. J. Protective Struct.* 1(4), 489–506 (2010).

[22] Arbitrary Lagrangian–Eulerian Methods, Encyclopedia of Computational Mechanics, eds. Stein E, de Borst R and Hughes TJR. Volume 1: *Fundamentals*. John Wiley & Sons, 2004

[23] LS-DYNA Manual, http://www.dynasupport.com/news/ls-dyna-971-manual-pdf [accessed 10.10.2018].

[24] D.J. Steinberg, "Equation of state and strength properties of selected materials", *Lawrence Livermore National Library* (1996).

[25] S. Stanislawek, A. Morka, and T. Niezgoda, "Pyramidal ceramic armor ability to defeat projectile threat by changing its trajectory", *Bull. Pol. Ac.: Tech.* 63(4), 843–49 (2015).